

Low-dose phase contrast tomography with conventional x-ray sources

C. K. Hagen, P. R. T. Munro, M. Endrizzi, P. C. Diemoz, and A. Olivo

Citation: *Medical Physics* **41**, 070701 (2014); doi: 10.1118/1.4884297

View online: <http://dx.doi.org/10.1118/1.4884297>

View Table of Contents: <http://scitation.aip.org/content/aapm/journal/medphys/41/7?ver=pdfcov>

Published by the [American Association of Physicists in Medicine](#)

Articles you may be interested in

[X-ray scatter correction method for dedicated breast computed tomography](#)

Med. Phys. **39**, 2896 (2012); 10.1118/1.4711749

[Development of a prototype gantry system for preclinical x-ray phase-contrast computed tomography](#)

Med. Phys. **38**, 5910 (2011); 10.1118/1.3644844

[Radiation dose efficiency comparison between differential phase contrast CT and conventional absorption CT](#)

Med. Phys. **37**, 2473 (2010); 10.1118/1.3425785

[Investigation of lung nodule detectability in low-dose 320-slice computed tomography](#)

Med. Phys. **36**, 1700 (2009); 10.1118/1.3112363

[Visibility of microcalcification in cone beam breast CT: Effects of x-ray tube voltage and radiation dose](#)

Med. Phys. **34**, 2995 (2007); 10.1118/1.2745921



WHAT IF YOU COULD
CONNECT EVERYTHING?

All-in-One. All Connected. All Secure.

Protect,
enhance
and save
lives
iba

Medical Physics Letter

Low-dose phase contrast tomography with conventional x-ray sources

C. K. Hagen^{a)}

Department of Medical Physics and Bioengineering, University College London, Malet Place, Gower Street, London WC1E 6BT, United Kingdom

P. R. T. Munro

Optical + Biomedical Engineering Laboratory, School of Electrical, Electronic and Computer Engineering, The University of Western Australia, 35 Stirling Highway, Crawley, Western Australia 6009, Australia and Centre for Microscopy, Characterisation, and Analysis, The University of Western Australia, 35 Stirling Highway, Crawley, Western Australia 6009, Australia

M. Endrizzi, P. C. Diemoz, and A. Olivo

Department of Medical Physics and Bioengineering, University College London, Malet Place, Gower Street, London WC1E 6BT, United Kingdom

(Received 31 March 2014; revised 13 May 2014; accepted for publication 4 June 2014; published 24 June 2014)

Purpose: The edge illumination (EI) x-ray phase contrast imaging (XPCi) method has been recently further developed to perform tomographic and, thus, volumetric imaging. In this paper, the first tomographic EI XPCi images acquired with a conventional x-ray source at dose levels below that used for preclinical small animal imaging are presented.

Methods: Two test objects, a biological sample and a custom-built phantom, were imaged with a laboratory-based EI XPCi setup in tomography mode. Tomographic maps that show the phase shift and attenuating properties of the object were reconstructed, and analyzed in terms of signal-to-noise ratio and quantitative accuracy. Dose measurements using thermoluminescence devices were performed.

Results: The obtained images demonstrate that phase based imaging methods can provide superior results compared to attenuation based modalities for weakly attenuating samples also in 3D. Moreover, and, most importantly, they demonstrate the feasibility of low-dose imaging. In addition, the experimental results can be considered quantitative within the constraints imposed by polychromaticity.

Conclusions: The results, together with the method's dose efficiency and compatibility with conventional x-ray sources, indicate that tomographic EI XPCi can become an important tool for the routine imaging of biomedical samples. © 2014 American Association of Physicists in Medicine. [<http://dx.doi.org/10.1118/1.4884297>]

Key words: tomography, x-rays, phase contrast

1. INTRODUCTION

X-ray phase contrast imaging (XPCi) has become an important tool for the nondestructive visualization of weakly attenuating samples as often encountered in biomedical applications. The dominant contrast mechanism is the phase shift of x-rays as they traverse a sample, as opposed to attenuation which is used in conventional radiography. Both effects are described by the complex refractive index:

$$n(E) = 1 - \delta(E) + i\beta(E), \quad (1)$$

where δ and β are responsible for the phase shift and attenuation, respectively, and E is the x-ray photon energy. For biological tissues, δ can be up to three orders of magnitude larger than β .¹ Hence, XPCi methods can provide superior contrast for many soft tissue specimens.¹

Different XPCi methods exist, both as planar and computed tomography (CT) modalities,²⁻⁸ and all of them are compatible with microfocal and/or synchrotron radiation

x-ray sources. Several techniques have been demonstrated to be also compatible with standard (nonmicrofocal) x-ray sources.⁹⁻¹³ This compatibility is crucial to meet the needs of many biological disciplines (e.g., small animal imaging), for example, to perform scans in standard research laboratories, fast, repeatedly, and with a high throughput.

The Edge Illumination (EI) XPCi method has the potential to meet this need since, as well as working with standard x-ray sources,¹⁰ it is based on a simple setup, can be scaled up to large fields of view, is relatively immune to environmental vibrations, has a high phase sensitivity, and is dose efficient.¹⁴⁻¹⁸ While previously tomographic images acquired with a monochromatic synchrotron source were shown,⁸ in this paper, the first tomographic images obtained from an EI XPCi system implemented with a commercial laboratory x-ray tube are presented. The obtained results demonstrate the superiority of phase over attenuation based imaging, as well as the feasibility of imaging at doses well within the limits of

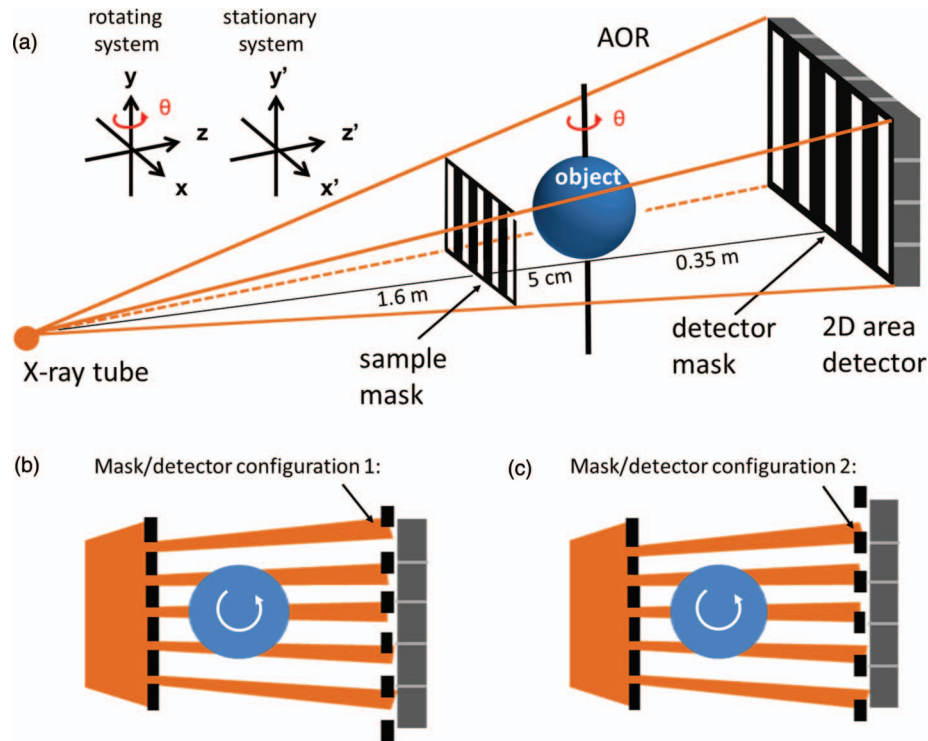


FIG. 1. Schematic of the experimental setup of the laboratory implementation of tomographic EI XPCi. (a) 3D view of the setup, [(b),(c)] views from top showing two opposing edge illumination conditions that can be achieved by shifting the sample mask appropriately.

what is considered acceptable for *in vivo*, e.g., small animal imaging applications. Moreover, by means of a phantom study, it is demonstrated that the obtained results are quantitative within the limits imposed by the use of a polychromatic source, along the lines discussed in Ref. 22. The results are presented and discussed in the supplementary material.²⁴

2. MATERIALS AND METHODS

Figure 1(a) shows a schematic of the laboratory implementation of EI XPCi. For a detailed explanation of the method's working principle, the reader is referred to previous publications.^{10,15,17} The method was adjusted for tomographic imaging by inserting a rotation axis parallel to the masks' apertures (orthogonal to the direction of phase sensitivity). If, at each rotation angle, two projections are acquired at opposing edge illumination configurations [Figs. 1(b) and 1(c)] and processed according to a dedicated algorithm,¹⁹ sinograms that contain the object's attenuation and the first derivative of the object's phase function, given by

$$S_{\hat{\delta}}(x, y; \theta) = \frac{1}{\hat{k}} \frac{\partial}{\partial x} \hat{\Phi}(x, y; \theta) = \frac{\partial}{\partial x} \int_{\ell(x, y; \theta; s)} \hat{\delta}(x', y', z') ds, \quad (2)$$

$$S_{\hat{\beta}}(x, y; \theta) = \hat{M}(x, y; \theta) = 2 \int_{\ell(x, y; \theta; s)} \hat{k} \hat{\beta}(x', y', z') ds \quad (3)$$

are obtained. The line $\ell(x, y; \theta; s)$ describes the path of an x-ray hitting the detector at (x, y) and \hat{k} is the wave number. From these sinograms, tomographic maps of $\hat{\delta}$ and $\hat{k} \hat{\beta}$ can be reconstructed with established methods,²⁰ noting that the derivative in Eq. (2) requires a specialized filter function.²¹

Please note that monochromatic radiation was not assumed and that the quantities indicated by the hat refer to an effective energy, i.e., $\hat{k} = k(E_{\text{eff}})$, $\hat{\delta} = \delta(E_{\text{eff}})$, and $\hat{\beta} = \beta(E_{\text{eff}})$. In EI XPCi, not only is the effective energy determined by the imaging system (source spectrum, detector response, masks), but also by the imaged object itself (thickness and attenuation), and phase and attenuation effective energies are, in general, different.²²

The spatial sampling rate of Eqs. (2) and (3) is normally limited by the (demagnified) pixel size; however, the sampling rate can be increased by “dithering,” i.e., shifting the object in the direction orthogonal to the masks' apertures by sub-pixel amounts, and taking multiple projections which are then combined. Dithering can reveal sub-pixel details which would not be captured in a single shot; however, it increases scan duration and sample exposure. If applied, dithering only increases the sampling rate within transverse slices of the object, while the sampling rate in the vertical direction (slice thickness) is still given by the vertical pixel size.

Our experimental setup employs the Rigaku MicroMax 007 HF rotating anode (molybdenum) x-ray tube (Rigaku Corporation, Japan), operated at 35 kVp and 25 mA. The size of the source's focal spot was measured to be $\sim 70 \mu\text{m}$. As a detector, the Anrad SMAM a-Se direct conversion flat panel (Analogic Canada Corporation, Canada) with a pixel size of $85 \mu\text{m}$ was used. The source-to-sample mask and sample mask-to detector distances were 1.6 and 0.4 m, respectively. The AOR was placed approximately 5 cm downstream the sample mask. In this practical setting, the detector mask was positioned approximately 4 cm before the detector. Both masks were fabricated by electroplating gold strips

onto a graphite substrate (Creatv Microtech Inc., Potomac, MD). The masks' periods were $66.8\ \mu\text{m}$ (sample mask) and $83.5\ \mu\text{m}$ (detector mask), with open fractions of 18% and 24%, respectively. All CT acquisitions were carried out over a total angular range of 180° with a 1° step. At each angle, projections were acquired with either 32, two or no dithering steps (no object displacement), and were taken at opposing edge illumination conditions, with the sample mask positioned such that 50% of each beamlet falls onto the uncovered pixel area [Figs. 1(b) and 1(c)]. The data processing involved the recombination of dithered (if present) into single projections and phase retrieval according to Ref. 19, yielding sinograms in form of Eqs. (2) and (3). For CT reconstruction, filtered back-projection (FBP) was employed using Hilbert and ramp filters for the phase and attenuation maps, respectively.

A biological specimen (a common wasp), as well as a custom-built phantom (see the supplementary material²⁴), were chosen as test objects. Most acquisitions were performed with 5 s exposure time per projection and dithering step and without any additional source filtration. For the nondithered acquisition of the wasp, the exposure time was 3 s and a $30\ \mu\text{m}$ molybdenum filter was used to demonstrate the low-dose capabilities of the system. The entrance dose (air kerma) resulting from the filtered spectrum was measured by means of thermoluminescence devices (TLD-100H), placed at the position of the object. The TLDs were calibrated in air kerma against a reference ion chamber. The measurements were repeated with an independent ion chamber (Keithley 35050A) and the same entrance doses were obtained within $\sim 10\%$ accuracy.

3. RESULTS AND DISCUSSION

Figures 2–4 show the reconstructed CT images of the wasp. In Fig. 2, coronal slices showing the head and thorax of the insect are rendered, which were extracted from the reconstructed δ - (a) and $\hat{k}\hat{\beta}$ -maps (b). In this case, the projections were acquired with 32 dithering steps. Profiles across the torso, plotted underneath, confirm the expected superior-

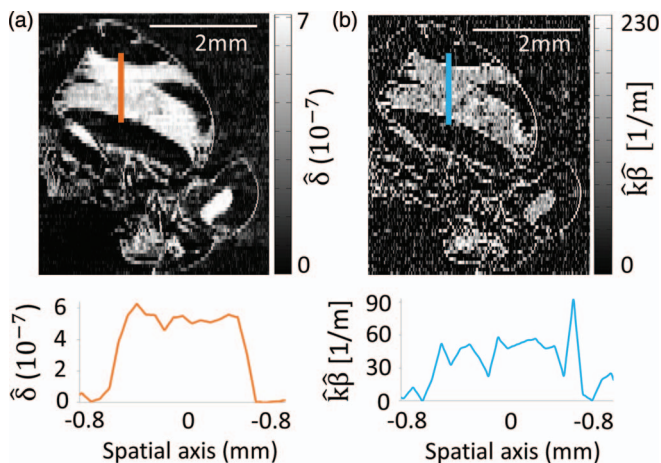


FIG. 2. Tomographic images (coronal slices) of a wasp showing δ (a) and $\hat{k}\hat{\beta}$ (b) within the insect. Profiles extracted across the indicated thorax region are plotted below.



FIG. 3. Volume rendering of the δ -map for a wasp (head and thorax region only), reconstructed from data acquired with 32 dithering steps.

ity of the signal difference-to-noise ratio (SDNR) in the phase image (SDNR = 18.42) compared to that in the attenuation image (SDNR = 4.91). The SDNR was calculated according to the formula:

$$SDNR = \frac{\text{Signal}_{\text{feature}} - \text{Signal}_{\text{background}}}{\sigma_{\text{background}}}, \quad (4)$$

where σ denotes the standard deviation. The signal and σ of the background were calculated for the less dense part of the wasp adjacent to the torso.

Figure 3 shows a volume rendering of the reconstructed δ -map, created with the open-source software 3DSlicer (www.slicer.org). Small features such as the antennas and the structure of the head and thorax are clearly visible. The high level of detail resulted from the high number of dithering steps.

Figure 4 shows transverse [(a)–(c)] and coronal [(e)–(g)] slices, showing the insect's thorax only and both head and thorax, respectively, extracted from δ -maps reconstructed from data which were acquired with different numbers of dithering steps (32, two, and none) and, hence, reveal different levels of detail. This difference is clearer in the transverse slices, since dithering is only a means to increase the sampling rate within, but not across slices. A very high level of detail, revealing the fine structures inside the insect's head, can be appreciated in Fig. 4(a), which was acquired with 32 dithering steps, i.e., with a comparatively high sampling rate. Besides the differing levels of detail, it is noteworthy that the reconstructed δ -values are similar in all images. This indicates that the signal strength in the δ -maps is not affected by the sampling rate.

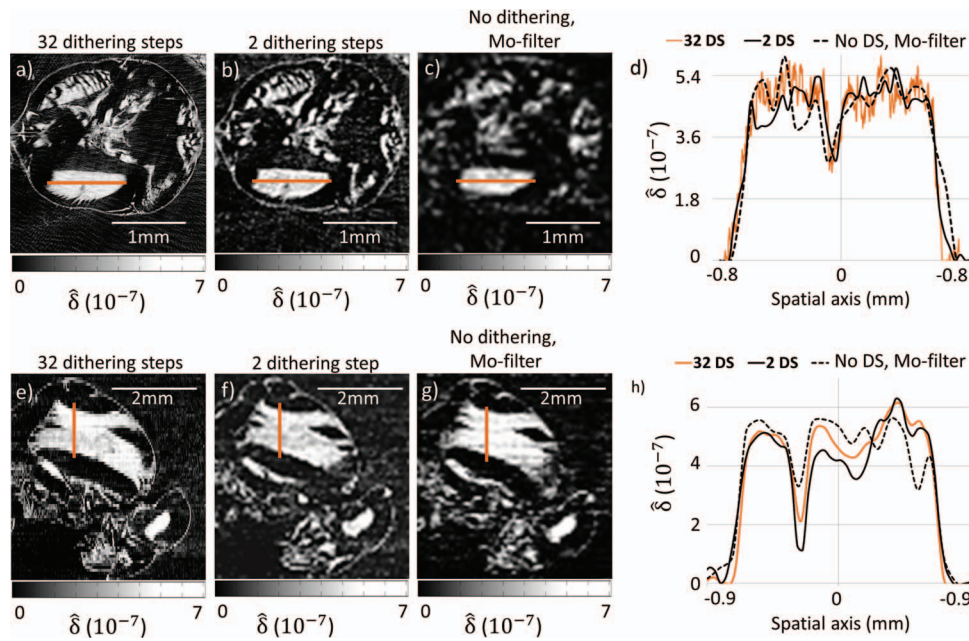


FIG. 4. Transverse [(a)–(c)] and coronal [(e)–(g)] slices extracted from the reconstructed δ -maps of a wasp, showing the thorax and both head and thorax, respectively. The maps originate from data acquired with 32, two, or no dithering steps. The plots in (d) and (h) show the profiles extracted across the horizontal and vertical lines indicated in the images.

The profiles extracted across the indicated trajectories in the transverse and coronal slices, plotted in Figs. 4(d) and 4(h), confirm this observation, since all curves have a similar magnitude. Although the nondithered images [(c), (g)] were acquired with additional molybdenum filtration to prevent the low end of the polychromatic spectrum from contributing to the delivered dose, the signal is as high as for 32 and two dithering steps, where no additional filtration was used. The profiles again confirm that dithering only has an effect on the sampling rate within the transverse slices. While in Fig. 4(d) the highly dithered profile (orange line) reveals much finer structures than the profiles originating from the data acquired with two and no dithering steps (black and black dotted lines), all three profiles in Fig. 4(h) show a similar level of detail.

The observation that, while the degree to which fine structures can be resolved is reduced, on average the values in the δ -maps remain unaffected when little or no dithering is employed, provides the option for fast and low-dose imaging. The entrance dose with the molybdenum filtration was measured to be 0.043 mGy per 1 s exposure time. Assuming an acquisition with 180 rotation angles, no dithering and 3 s exposure time per projection [i.e., the acquisition parameters effectively used for the images shown in Fig. 4(c) and 4(g)], the total entrance dose would be approximately 46 mGy, about a tenth of the limits imposed by small animal imaging.²³ Please note that this number already includes the factor of two taking into account that two projections need to be acquired at each angle at opposing edge illumination configurations. In a configuration where the mask apertures are orthogonal to the rotation axis, which would enable performing CT reconstructions without phase retrieval, this dose could be further halved at least in cases where edge-enhanced rather than fully phase-retrieved images could be considered sufficient.⁸ It should be noted that the degree of resolution obtained without dithering

[Figs. 4(c) and 4(g)] is already compatible with current small animal scanners: our approach leaves the option to increase the number of dithering steps and rotation angles in order to improve the resolution of the reconstructed maps, or the exposure time in order to increase the CNR, plus a range of possible combinations of the two/intermediate solutions, still at acceptable doses. The dose efficiency of EI XPCi has already been observed previously,¹⁸ and can be explained by the fact that the sample mask is located upstream of the object, i.e., the object is shielded from radiation that does not contribute to the image formation process. The fact that the masks' substrate is made of low-absorbing graphite is also beneficial with respect to dose efficiency, as unnecessary photon absorption by the detector mask is avoided.

4. CONCLUSION

The first tomographic images obtained with the laboratory implementation of EI XPCi were presented. The experimental setup comprised a commercial x-ray source with an extended nonmicrofocal spot and a polychromatic spectrum. It was observed that maps showing the phase shifting properties of an object provided a higher SDNR than attenuation maps. Further, the effect of object dithering, i.e., an increase in sampling rate and the consequential improved detail visibility, was highlighted and shown that dithering does not affect the signal strength. Accurate results were obtained also using filters to reduce the dose delivered to the sample, providing an option for low-dose imaging. The entrance dose with the additional source filtration was measured and found to be approximately ten times below that considered acceptable for small animal imaging. Finally, the quantitiveness (within the limits of polychromaticity) of the imaging system was tested by scanning a phantom of known materials

and by comparing retrieved phase and attenuation properties with theoretical ones, and a good agreement for most materials was found (see the supplementary material).²⁴ The results of this paper indicate that tomographic EI XPCi can become an important tool for laboratory-based and, hence, for high throughput imaging of biomedical samples, e.g., small animal models.

ACKNOWLEDGMENTS

This work was supported by the UK Engineering and Physical Sciences Research Council (Grant Nos. EP/L001381/1 and EP/I021884/1). P.C.D. and M.E. are supported by Marie Curie Career Integration Grant Nos. PCIG12-GA-2012-333990 and PCIG12-GA-2012-334056 within the Seventh Framework Programme of the European Union. P.R.T.M. is supported by a Discovery Early Career Research Award from the Australian Research Council (DE120101331).

^{a)}Electronic mail: charlotte.hagen.10@ucl.ac.uk

- ¹R. Lewis, C. Hall, A. Hufton, S. Evans, R. Menk, F. Arfelli, L. Rigon, G. Tromba, D. Dance, I. Ellis, A. Evans, E. Jacobs, S. Pinder, and K. Rogers, "X-ray refraction effects: Application to the imaging of biological tissues," *Br. J. Radiol.* **76**, 301–308 (2003).
- ²A. Bravin, P. Coan, and P. Suortti, "X-ray phase contrast imaging: From pre-clinical applications towards clinics," *Phys. Med. Biol.* **58**, R1–R35 (2013).
- ³A. Momose, T. Takeda, Y. Itai, and K. Hirano, "Phase-contrast x-ray computed tomography for observing biological soft tissues," *Nat. Med.* **2**(4), 473–475 (1996).
- ⁴P. Cloetens, W. Ludwig, J. Baruchel, D. Van Dyck, J. Van Landuyt, J. P. Guigay, and M. Schlenker, "Holotomography: Quantitative phase tomography with micrometer resolution using hard synchrotron radiation x-rays," *Appl. Phys. Lett.* **75**(19), 2912–2914 (1999).
- ⁵F. Dilmanian, Z. Zhong, B. Ren, X. Wu, L. Chapman, I. Orion, and W. Thomlinson, "Computed tomography of x-ray index of refraction using the diffraction enhanced imaging method," *Phys. Med. Biol.* **45**, 933–946 (2000).
- ⁶T. Weitkamp, A. Diaz, C. David, F. Pfeiffer, M. Stampanoni, P. Cloetens, and E. Ziegler, "X-ray phase imaging with a grating interferometer," *Opt. Express* **13**(16), 6296–6304 (2005).
- ⁷P. Zhu, K. Zhang, Z. Wang, Y. Liu, X. Liu, Z. Wu, S. A. McDonald, F. Marone, and M. Stampanoni, "Low-dose, simple, and fast grating-based x-ray phase-contrast imaging," *Proc. Natl. Acad. Sci. U.S.A.* **107**(31), 13576–13581 (2010).
- ⁸C. K. Hagen, P. C. Diemoz, M. Endrizzi, L. Rigon, D. Droessi, F. Arfelli, F. C. M. Lopez, R. Longo, and A. Olivo, "Theory and preliminary experimental verification of quantitative edge illumination x-ray phase contrast tomography," *Opt. Express* **22**(7), 7989–8000 (2014).
- ⁹F. Pfeiffer, T. Weitkamp, O. Bunk, and C. David, "Phase retrieval and differential phase contrast imaging with low-brilliance x-ray sources," *Nat. Phys.* **2**, 258–261 (2006).
- ¹⁰A. Olivo and R. Speller, "A coded-aperture technique allowing x-ray phase contrast imaging with conventional sources," *Appl. Phys. Lett.* **91**, 074106 (2007).
- ¹¹N. Bevins, J. Zambelli, K. Li, Z. Qi, and G. Chen, "Multicontrast x-ray computed tomography imaging using Talbot-Lau interferometry without phase stepping," *Med. Phys.* **39**(1), 424–428 (2012).
- ¹²H. Wen, E. E. Bennett, M. M. Hegedus, and S. Rapcchi, "Fourier x-ray scattering radiography yields bone structural information," *Radiology* **251**(3), 910–918 (2009).
- ¹³C. Parham, Z. Zhong, D. M. Connor, D. Chapman, and E. Pisano, "Design and implementation of a compact low-dose diffraction enhanced medical imaging system," *Acad. Radiol.* **16**(8), 911–917 (2009).
- ¹⁴A. Olivo, F. Arfelli, G. Cantatore, R. Longo, R. Menk, S. Pani, M. Prest, P. Poporat, L. Rigon, G. Tromba, E. Vallazza, and E. Castelli, "An innovative digital imaging set-up allowing a low-dose approach to phase contrast applications in the medical field," *Med. Phys.* **28**(8), 1610–1619 (2001).
- ¹⁵T. P. Millard, M. Endrizzi, K. Ignatyev, C. K. Hagen, P. R. T. Munro, R. Speller, and A. Olivo, "Method for the automatization of the alignment of a laboratory based x-ray phase contrast edge illumination system," *Rev. Sci. Instrum.* **84**, 083702 (2013).
- ¹⁶P. C. Diemoz, M. Endrizzi, C. E. Zapata, Z. Pesic, C. Rau, A. Bravin, I. Robinson, and A. Olivo, "X-ray phase contrast imaging with nanoradian angular resolution," *Phys. Rev. Lett.* **110**, 138105 (2013).
- ¹⁷P. C. Diemoz, C. K. Hagen, M. Endrizzi, and A. Olivo, "Sensitivity of laboratory based implementations of edge illumination x-ray phase-contrast imaging," *Appl. Phys. Lett.* **103**, 244104 (2013).
- ¹⁸A. Olivo, S. Gkoumas, M. Endrizzi, C. K. Hagen, M. B. Szafraniec, P. C. Diemoz, P. R. T. Munro, K. Ignatyev, B. Johnson, J. A. Horrocks, S. J. Vinnicombe, J. L. Jones, and R. D. Speller, "Low-dose phase contrast mammography with conventional sources," *Med. Phys.* **40**(9), 090701 (6pp.) (2013).
- ¹⁹P. R. T. Munro, C. K. Hagen, M. B. Szafraniec, and A. Olivo, "A simplified approach to quantitative coded aperture x-ray phase imaging," *Opt. Express* **21**(9), 11187–11201 (2013).
- ²⁰A. C. Kak and M. Slaney, *Principles of Computerized Tomographic Imaging* (IEEE Press, New York, NY, 1988).
- ²¹Z. Huang, K. Kang, Z. Li, P. Zhu, Q. Yuan, W. Huang, J. Huang, D. Zhang, and A. Yu, "Direct computed tomographic reconstruction for directional-derivative projections of computed tomography of diffraction enhanced imaging," *Appl. Phys. Lett.* **89**, 041124 (2006).
- ²²P. R. T. Munro and A. Olivo, "X-ray phase contrast imaging with polychromatic sources and the concept of effective energy," *Phys. Rev. A* **87**, 053838 (2013).
- ²³R. E. Guldberg, A. S. P. Lin, R. Coleman, G. Robertson, and C. Duvall, "Microcomputed tomography imaging of skeletal development and growth," *Birth Defects Res. C* **72**, 250–259 (2004).
- ²⁴See supplementary material at <http://dx.doi.org/10.1118/1.4884297> for an assessment of the quantitative accuracy of tomographic EI XPCi measurements with a polychromatic x-ray tube.